Slope-Weighted Eccentricity: Automatic Terrain Classification of Atlantic Ocean Crust

Gabriella Alodia[1], Christopher Green[2], Andrew McCaig[1], and Douglas Paton[1]

[1]University of Leeds
[2]University of Leeds, Getech Group plc

November 28, 2022

Abstract

The shapes and directionality of bathymetry at slow-spreading ridges are key to understanding the magmatic or tectonic emplacement of the crust. Magmatic terrain is marked by linearly fault-bounded abyssal hills, while tectonic terrain is marked by long-lived detachment faults, forming Oceanic Core Complexes (OCCs). However, the quantitative description of these crustal regimes is still limited. We develop a novel automated terrain classification technique and test it at the 13-15° N section of the Mid-Atlantic Ridge. The algorithm uses the Slope-Weighted Eccentricity (SWE) of the horizontal eigenvalues to represent surface directionality and reveal crustal tectonic fabric. The application of this new technique yields results consistent with qualitative interpretation. Thus, it provides both new insights into the mid-oceanic ridge spreading and the potential to automate such mapping with different sets of grids, such as gravity and magnetic data in regions further away from the ridge where sediments mask sea-bed features.

Slope-Weighted Eccentricity: Automatic Terrain Classification of Atlantic Ocean Crust

G. Alodia[1], C. M. Green[1,2], A. M. McCaig[1], and D. A. Paton[1]

[1]School of Earth and Environment, University of Leeds, Leeds, UK

[2]GETECH, plc., Leeds, UK

Corresponding author: Gabriella Alodia (eega@leeds.ac.uk)

Key Points:

- We developed a novel automatic terrain classification technique derived from bathymetry to identify detachment and magmatic spreading
- The types of terrains are defined from the shape, directionality, and curvature of the crustal structure in high-resolution bathymetry

Abstract

The shapes and directionality of bathymetry at slow-spreading ridges are key to understanding the magmatic or tectonic emplacement of the crust. Magmatic terrain is marked by linearly fault-bounded abyssal hills, while tectonic terrain is marked by long-lived detachment faults, forming Oceanic Core Complexes (OCCs). However, the quantitative description of these crustal regimes is still limited. We develop a novel automated terrain classification technique and test it at the 13-15° N section of the Mid-Atlantic Ridge. The algorithm uses the Slope-Weighted Eccentricity (SWE) of the horizontal eigenvalues to represent surface directionality and reveal crustal tectonic fabric. The application of this new technique yields results consistent with qualitative interpretation. Thus, it provides both new insights into the mid-oceanic ridge spreading and the potential to automate such mapping with different sets of grids, such as gravity and magnetic data in regions further away from the ridge where sediments mask sea-bed features.

Plain Language Summary

The features of the ocean floor hold the key to understanding its evolution. At a slow-spreading ridge, this evolution is marked by two different types of seafloor. Linearly-aligned hills mark the history of magmatic activity while sporadic massifs, or the Oceanic Core Complexes (OCCs), represent a more tectonic regime. These two features are widely known, yet their quantitative description is still limited. Thus, we develop a novel technique by examining variation in the depth of the ocean floor, known as bathymetry, to reveal its underlying origin. The results are classified based on the general directionality and curvature of the seafloor features, described by the so-called “Slope-Weighted Eccentricity” (SWE). This technique will serve as an efficient way to automatically interpret the evolution of the ridge to understand further the processes at a slow-spreading ridge, which application can potentially be extended to gravity and magnetic data to identify features buried by sediments.

1 Introduction

Oceanic Core Complexes (OCCs) are seafloor domes in which lower-crustal and upper-mantle rocks are exhumed (e.g., Blackman et al., 2009; Cann et al., 1997; Dannowski et al., 2010; MacLeod et al., 2002; Smith et al., 2008). These exposures of deep-seated rocks have been a topic of interest since they mark a potentially large amount of tectonic extension at slow-spreading ridge segments, specifically in the Central Atlantic (Smith et al., 2006; Smith et al., 2008). The morphology in parts of the Central Atlantic contrasts with the linearly fault-bounded abyssal hills resulting from typical magmatic accretion (MacLeod et al., 2009; Sinton and Detrick, 1992), hence marking the complex interaction between magmatic accretion and tectonic extension in the area (Escartín and Cannat, 1999).

The formation of OCCs is initiated by a local waning of magma supply below a critical threshold (MacLeod et al., 2009). The local waning triggers the thinning of the crustal layer that allows the formation of secondary hydrous minerals such as talc and serpentine, which in turn causes weakening of the lithosphere along the axis (Escartín et al., 1997; Escartín et al., 2001). Some faults then experience strain localization from this lithosphere weakening before they are rotated and create a long-lived fault at the footwall, often with corrugation parallel to the spreading direction (Buck, 1988; Cann et al., 1997; Reston and Ranero, 2011). This rotation forms a low-angle and curved fault as a response to the flexural unloading during extension (Buck, 1988; Buck et al., 2005; Lavier et al., 1999; Tucholke et al., 2008). Mantle lithosphere is then brought up to shallower levels following the rotation, marking a sharp discontinuity between the exhumed mantle rocks and the surrounding upper-crust rocks, hence the term “detachment spreading” (McCaig and Harris, 2012).

Initially considered to only form at inside corners of fracture zones (FZs), the growing discovery of OCCs away from the axis (Cann et al., 1997) has postulated questions over their general distribution as they were found in crust as old as 10 Ma (e.g., Cann et al., 2015). However, with the limited distribution d of dredged, drilled, and submersible samples (Cannat et al., 1992; Lagabrielle et al., 1998; Schroeder et al., 2007), the identification that has been attempted over the years is mostly based on qualitative observation of the high-resolution bathymetry. This study aims to automate the identification processes by quantifying characteristics of both magmatic and detachment spreading. The algorithm is based on the parameterization of the shape, directionality, and curvature of the seafloor. The automatic seafloor definition will then act as a novel tool to provide new insight into slow-spreading ridge processes through time and is potentially ready to be applied at different parts of the ridge.

2 Bathymetry and Tectonic Setting

We selected an area with high-resolution bathymetry data over ~5 Ma (Escartín and Cannat, 1999; Fujiwara et al., 2003; Smith et al., 2006) between the Marathon and Fifteen-Twenty FZs (13-15° N) as our study site (Figure 1a). The combined bathymetry was gridded with 200 m resolution. The area represents a complex history of magmatism and tectonism from the movement of the North American (NA), South American (SA), and African (AF) plates (e.g., Bonatti, 1996; Müller and Smith, 1993). Located in the Central Atlantic, the site has been speculated as a potential location of the NA-SA-AF triple junction (Escartín et al., 2003).

Seismicity in the area has been recorded by an array of hydrophones (Smith et al., 2003; Smith et al., 2002), in which the recorded earthquake events were declustered according to their potential mainshock-aftershock sequence (Olive and Escartín, 2016). The earthquake distribution in the study site reflects its tectonism, where continuous seismicity is found close to the bounding FZs while a seismic gap is found in the middle of the site (Escartín et al., 2003). The seismic gap at the 14° N segment is consistent with a continuous zone of high acoustic backscatter as well as a magmatically-robust morphology, marked by the presence of long abyssal hills parallel to the spreading axis, while the continuous seismicity at the 13° and 15° N segments occurred at a terrain with much rougher topography where sporadic massifs are in place (Smith et al., 2008). The abundant samples of ultramafic rocks close to these massifs at both 13° and 15° N segments (e.g., Cannat et al., 1997; MacLeod et al., 2009; Rona et al., 1987) demonstrates the domination of the OCC formation specifically in these two segments (Smith et al., 2008). The formation is accommodated through detachment faulting and is linked both to the limited magma supply and increased tectonic strain (MacLeod et al., 2009). The distinct morphology of both magmatic and detachment modes of spreading at the 13-15° N segments makes it a suitable site to assess the automated classification algorithm.

In this study, we resampled the bathymetry into 8’ (~14.8 km) grids with 15” (~450 m) grid spacing to assess the algorithm at small patches of terrain (insets in Figure 1). The grid size is chosen based on the average size of OCCs found at the MAR, while the resolution allows us to have a closer look at the morphology and as well as the distribution of the slope and directionality (aspect) of both magmatic abyssal hills and domed OCCs. We then created a coarser resolution of 30” grid of the whole study area to allow the algorithm to run more efficiently while still capturing the general morphology of the seafloor. The algorithm is based on the statistics of specific parameters that depict the shapes and directionality of the seafloor, which in this study is termed as Slope-Weighted Eccentricity (SWE) in Figure 1b.

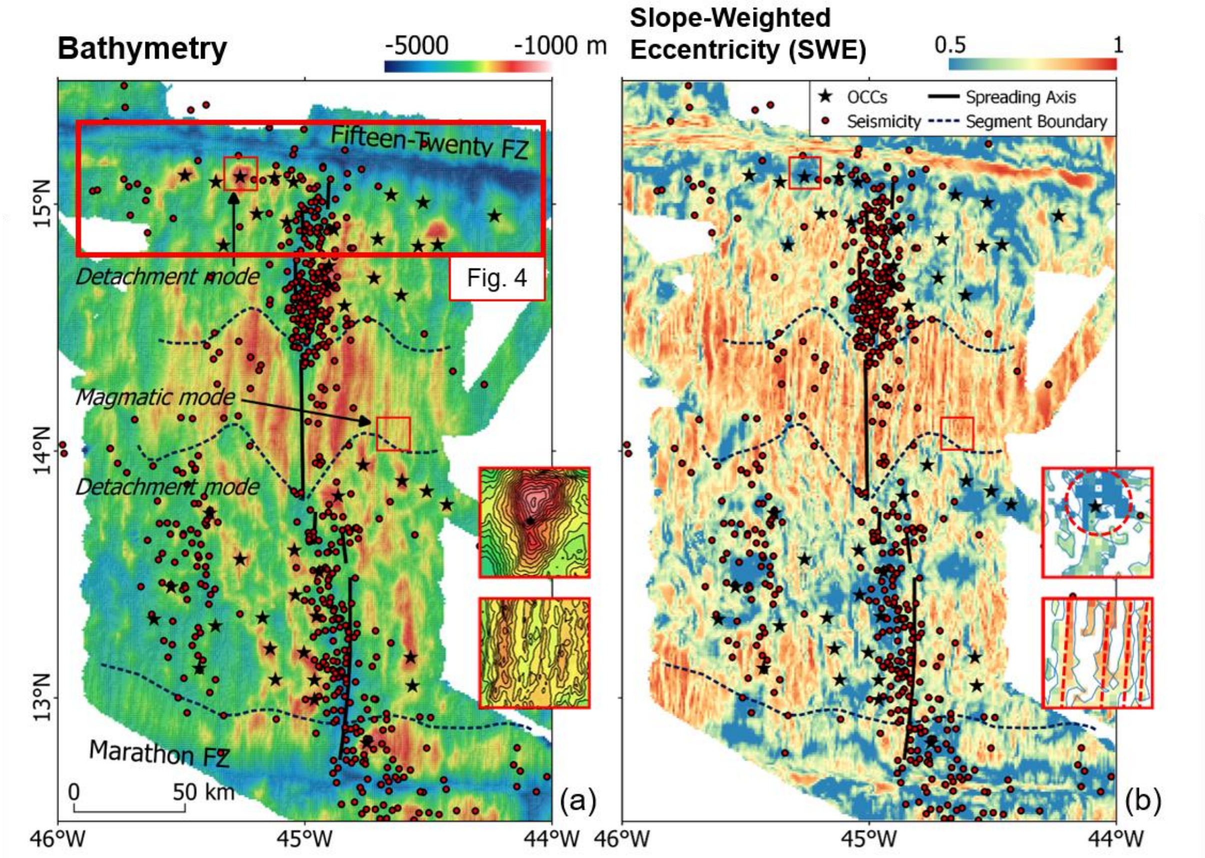

Figure 1 (a) Bathymetry of the study site gridded at 30” resolution (Escartín and Cannat, 1999; Fujiwara et al., 2003; Smith et al., 2006). Black stars: inferred OCCs (Smith et al., 2008). Red dots: declustered seismicity (Olive and Escartín, 2016). Black thick lines: spreading axes. Dark blue dashed lines: segment boundaries. The squares with red lines indicate the two small patches of seafloor representing detachment and magmatic modes. Detachment mode is depicted as dome-shaped OCCs, while the magmatic mode is depicted as linear abyssal hills. (b) Slope-Weighted Eccentricity (SWE) with the same grid spacing as the bathymetry. Lower values mark the presence of detachment spreading, while higher values represent a more magmatic regime. See Section 3 for an explanation of the algorithm.

3 Algorithm Building

3.1. Spherical Distribution and Eigenvalues

We created two small synthetic models that mimic the topographical extremes of both types of spreading, i.e., linear abyssal hills for magmatic spreading (Figure 2a) and a circular dome for detachment spreading (Figure 2b). For the synthetic magmatic terrain, we constructed East-West dipping abyssal hills, mimicking the direction of the slopes at the 14° N segment, while for the synthetic OCC we constructed a hemisphere with diameter 8’. Real world data from both terrains were resampled into the same size and grid spacing as the two synthetic models (Figure 2c, 2d). The patches were chosen as the sampled magmatic terrain hosts a series of long-wavelength abyssal hills, while the sampled OCC has been described as one of the prominent OCCs in the area with several ultramafic rocks sampled around it (Escartín and Cannat, 1999; Fujiwara et al., 2003; Smith et al., 2008). Using this grid size, the OCC can be pictured as a single domed-massif. The resolution allows us to examine the slopes and directionality of each patch in detail.

We determined the parameters by assessing the statistics of the computed slopes (θ) and aspects (α) of each grid (Figure 2). The slopes and aspects of the synthetic magmatic terrain (Figure 2a) vary rapidly, while at the synthetic OCC (Figure 2b), we observe a more subtle variation. Consistent with the synthetic data, the magmatic terrain from the bathymetry (Figure 2c) shows a rapid change of both the slopes and aspects, which depict the steep yet short-lived scarps facing the spreading axis (Escartín and Cannat, 1999; Fujiwara et al., 2003; Smith et al., 2008). These steep, short-lived scarps contrast with the domed massif that characterizes detachment fault as the convex-downward morphology depicts the flexural rotation of the long-lived footwall. The remaining massif, or the OCC (Figure 2d), serves as a remnant of this tectonic extension. In general, we can see a bidirectional east-west trend at the magmatic terrain and a more omnidirectional trend at the detachment terrain.

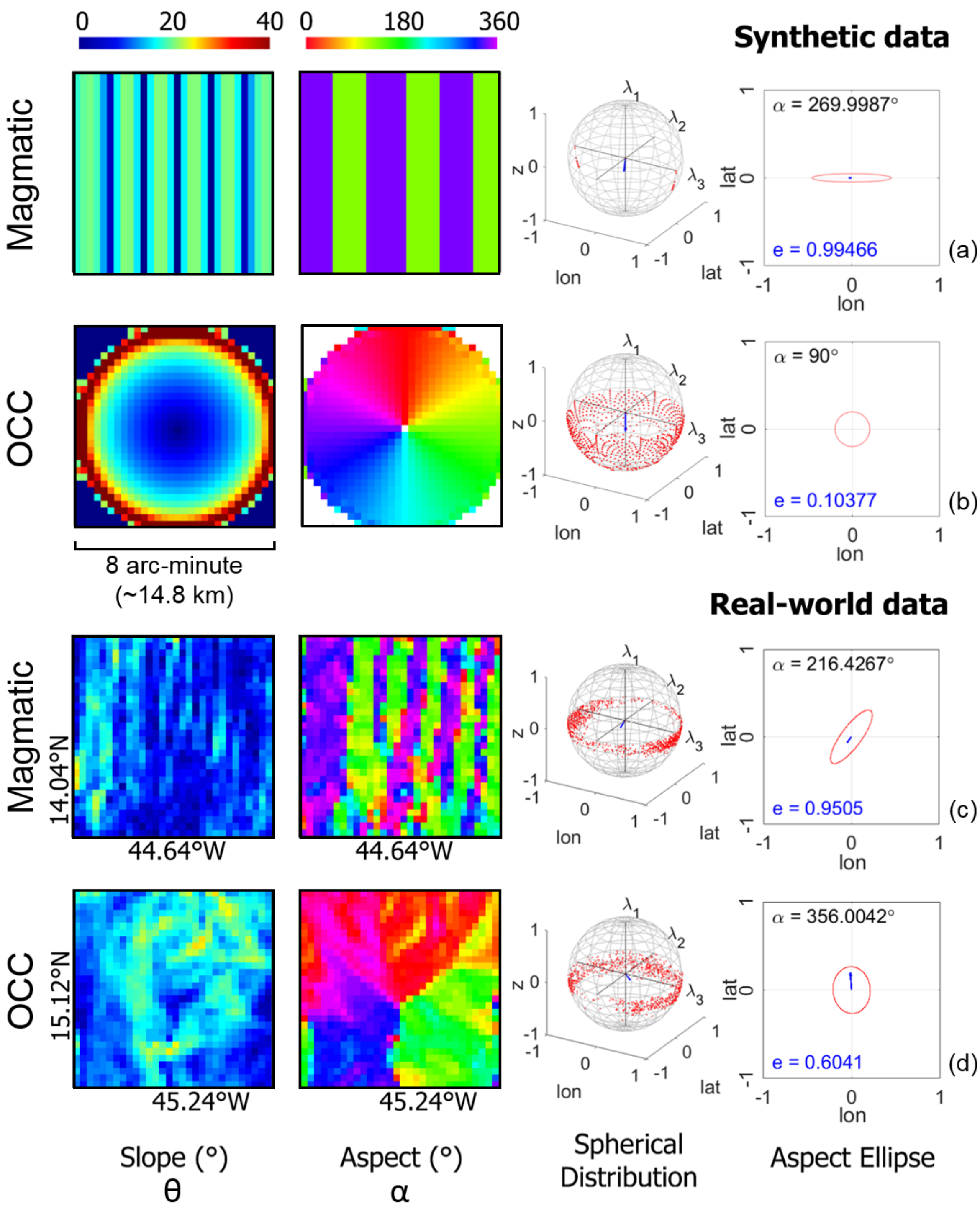

Figure 2 Slope (*θ*), aspect/directionality (*α*), spherical distribution, and aspect ellipse of (a) Synthetic magmatic terrain; (b) Synthetic OCC; (c) Real-world magmatic terrain, and; (d) Real-world OCC. All patches of terrain are 8’ in size with 15” grid spacing. Linear and rapidly alternating slopes govern the magmatic terrain, while it alternates more subtly over the OCC, highlighting its rounded shape. We observe a bidirectional trend at the aspect plot of the magmatic terrain while at the OCC, it is distributed in an omnidirectional form. Each cell (pixel) is plotted in a spherical distribution manner, simplified by the three eigenvalues representing the general pattern observed in each patch. We then compute an eccentricity (*e*) value from the horizontal eigenvalues (*λ2* and *λ3*) and plot the general horizontal directionality in the form of an “aspect ellipse.”

Having observed the directionality of both types of terrain in the form of slopes and aspects, we computed and plotted the sampled terrains as spherical distribution where:

$$x = \sin\alpha\cos\theta\ ;\ y = \cos\alpha\cos\theta\ ;\ z = \sin\theta \tag{1}$$

Each axis represents local longitude, latitude, and depth, respectively. All the 15" cells of the synthetic magmatic terrain plot at two opposite points, while the cells of the synthetic OCC are distributed almost evenly along the equator of the sphere. The three axes of the sphere are the eigenvalues, denoted λ_1, λ_2, and λ_3, which represent where about the moment of inertia of the point distribution is minimized or maximized (Watson, 1965; Woodcock, 1977). The minimum is denoted as λ_1. As observed, the variation in the vertical axis at both terrains is not comparable to the variation in the horizontal axis. Hence, the z-axis will always be where the moment of inertia is minimized, i.e., the λ_1. Following the right-hand rule, we define the λ_1, λ_2, and λ_3 as the eigenvalues representing the moment about the z-, x-, and y-axes, respectively. The sum of the three eigenvalues is always 1.

For the synthetic models, we compute eigenvalues of $\lambda_1 = 0.000$, $\lambda_2 = 0.010$, and $\lambda_3 = 0.990$ at the magmatic terrain (Figure 2a) while at synthetic OCC, the eigenvalues are $\lambda_1 = 0.004$, $\lambda_2 = 0.492$, and $\lambda_3 = 0.504$ (Figure 2b). These numbers are somewhat consistent with the real-world data, where we compute eigenvalues of $\lambda_1 = 0.027$, $\lambda_2 = 0.231$, and $\lambda_3 = 0.742$ at the magmatic terrain (Figure 2c) while at OCC, the eigenvalues are $\lambda_1 = 0.049$, $\lambda_2 = 0.422$, and $\lambda_3 = 0.529$ (Figure 2d). In general, we can see a greater difference between λ_2 and λ_3 at magmatic terrains compared to at OCCs, depicting a more clustered moment distribution at the magmatic terrains. As expected, λ_1 is relatively small for both terrains.

One of the most common approaches to represent the general classification of the pattern constructed by the point masses at the three axes is by computing the K-ratio (Woodcock, 1977), defined as $K = ln(\lambda_1/\lambda_2)/ln(\lambda_2/\lambda_3)$. However, as previously stated, the range of the slope is not comparable to the range of the aspect (0° to ~40° and 0° to 360°, respectively). If we use this ratio, the computed values will mainly represent the pattern observed at the horizontal axis, almost neglecting the vertical component. In addition, there is no known upper limit to the K-ratio, limiting the re-applicability of the algorithm at different settings as the range of the value is not fixed. Therefore, we developed a novel algorithm by first computing the pattern constructed by the point masses horizontally, then weight them based on the steepness and longevity of the slopes observed.

3.2. Slope-Weighted Eccentricity

We define the general directional pattern of the terrain by computing the eccentricity number (Equation 2) of the terrain patches from its two horizontal eigenvalues (λ_2 and λ_3). We use the term "aspect ellipse" to define the plotted results (Figure 2). We observe relatively high eccentricity (> 0.9) at both synthetic and real-world magmatic terrain, depicting a more significant difference between λ_2 and λ_3. In general, the aspect ellipse is a lot less flattened at both synthetic and real-world OCC as the values of λ_2 and λ_3 are relatively close for this type of terrain.

Having the algorithm tested in several terrain patches, we defined a range of eccentricity values to classify the terrain type based on its general directionality, with < 0.65 representing detachment terrain, 0.65-0.9 representing extended terrain, and > 0.9 representing magmatic terrain. Moreover, the fixed range of eccentricity values will make sure that the algorithm is re-applicable to different grid sets ($0 < e < 1$).

We then run the algorithm as a moving window on the whole grid, resampled at 30" grid spacing, which results can be seen in Figure 3a. The window size is optimized at 8' as it is typical of the average size of OCCs found at the MAR. From the results, we can already observe that the relatively omnidirectional trend is mostly found at ~13.5° N, ~15° N, and marked outer the edges of the fracture zones.

To introduce the vertical component, we created a weight matrix (W) by observing the slope distribution of the whole grid. OCCs are generally indicated by their long-lived fault, forming a domed morphology at the developed phase (e.g., MacLeod et al., 2009; Reston and Ranero, 2011). As discussed in Figure 2, these long-lived faults are depicted as steeper slopes compared to the short-lived faults that are not fully captured by the slope computation. Therefore, we can infer that the presence of the OCCs is typified by steep computed slopes. We fix the range of this parameter by computing its sine, so the values will always fall between 0 and 1. However, the results are inversely proportional to the initial classification, as OCCs are depicted in higher values of $sin(\theta)$. We multiply the eccentricity matrix by -sin(θ), hence the term "Slope-Weighted Eccentricity" where:

$$SWE = e * W = \sqrt{1 - \frac{(\lambda_2/2)^2}{(\lambda_3/2)^2}} * -\sin(\theta) \qquad (2)$$

The results from the SWE computation can be seen in Figure 3c and 1b, where the zonation of both detachment and magmatic mode of spreading is seen more clearly. The slope-based weight helps to highlight the texture of the structure, indicating the presence of potential faults and fissures. It also highlights the inner edges of the fracture zones, which automated the demarcation of this feature.

Although the algorithm seems to work in classifying the two different modes of spreading, it is still inadequate for interpreting individual OCCs, as the results are still independent of sign of curvature. For instance, an OCC is described similarly to an identical-sized basin, as the directionality of both structures is analogous. For that reason, we need to assess the curvature of the terrain to mask out the convex-upward structures from the grid.

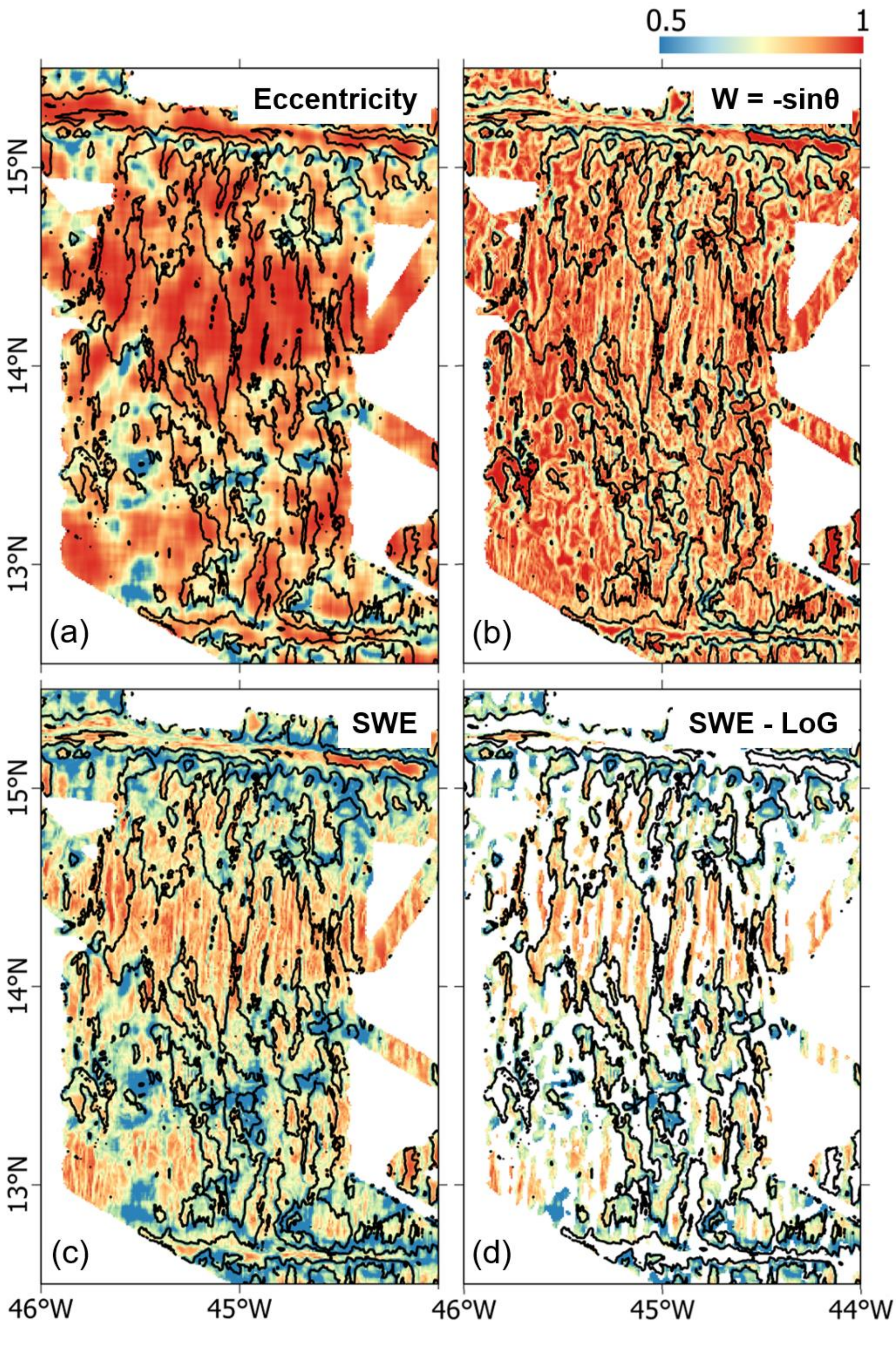

Figure 3 Illustration of the algorithm building. Contours of 1000 m are drawn in black lines. (a) Computed eccentricity values from bathymetry. This map can only identify terrain based on the horizontal directionality, neglecting the vertical component of the terrain. (b) We introduce the vertical component by computing the slope (θ) of the terrain, assigning weight (-sinθ). This way, we will have the values in the same fixed range as the eccentricity as well as having long-lived faults defined as detachments. (c) We assign -sinθ as the weight matrix of the eccentricity. The resulting SWE managed to classify the terrain into detachment (blue) and magmatic (red) terrains. (d) Laplacian-of-Gaussian mask (LoG) at 10 km low-pass wavelength cut-off was applied to mask out bathymetric lows from the SWE. The results can be used to identify individual OCCs.

3.2. Laplacian-of-Gaussian Mask

The convex-upward structures, or bathymetric lows, can be masked determining the zero-crossing of each slope from the bathymetry using the Laplacian filter (Marr and Hildreth, 1980). However, if the filter is applied directly to the original gridded bathymetry, too many edges will be detected as a slight change of slope will be defined as new zero-crossing. In the same study, Marr and Hildreth (1980) suggested the use of a smoothing filter before running the edge detection; hence the term Laplacian-of-Gaussian (LoG) mask (e.g., Huertas and Medioni, 1986). We run a 10-km low-pass Gaussian filter to smooth out the morphology of the seafloor, specifically at OCCs. The cut-off wavelength is optimized based on the average size of the OCCs at the study site. We then mask the SWE values where the LoG-filtered bathymetry is < 0. The final result can be seen in Figure 3d.

4 Results and Discussions

The automatic terrain classification from the SWE reflects the nature of magmatic accretion and tectonic extension in the region. In general, low SWE indicate and omnidirectional trend of the slope, while high numbers indicate a more bidirectional trend. In line with the classification from Smith et al. (2008), the terrain is divided into three segments, which are detachment segments at ~13.5° and ~15° N, and magmatic segments at ~13° N ~14.2° N. As mentioned, we defined three different ranges to classify the terrain based on its SWE, with < 0.65 representing detachment terrain, 0.65-0.9 representing extended terrain (Cann et al., 2015), and > 0.9 representing magmatic terrain. In Figure 1, we can see that the SWE map is consistent with what is observed by eye in the bathymetry as well as the seismicity pattern, where low SWE represent terrain with massifs interpreted as OCCs in Smith et al. (2008) and where more earthquakes are observed.

In this discussion, we will focus on the 15° N segment, where several OCCs have been identified, and several ultramafic samples have been taken. Firstly, we can see how the Gaussian filtering and Laplacian masking works by observing the terrain profile in Figure 4a. We can see how the interpreted OCCs in Figure 4b correlate with the general form of the terrain, termed here as ‘blue zone.’ In several places, interpreted OCCs are consistent with the sampled ultramafic rocks from previous studies, as seen in Figure 4c. The classification is also consistent with high Residual Mantle Bouguer Anomaly (RMBA) values from the same study (Figure 4c), implying thin crust in detachment terrains (Figure 4). The consistency leads to the possibility of applying the algorithm to gravity and magnetic data, to classify terrains at the ocean-continent transition where the oceanic crust is buried by sediment.

The algorithm works well at different parts of MAR, returning consistent results to the ranges that we have defined. However, the LoG mask depends entirely on the average size of OCCs we that we would like to see at specific segments. For instance, the average size of OCCs at 13-15° is around 10 km, while at 21-24° (the Mid-Atlantic Ridge at Kane, or MARK area), the average size is around 15 km. Hence, a general identification of the sizes of the OCCs that are clear by eye from the bathymetry is key to select the optimum cut-off wavelength for the mask.

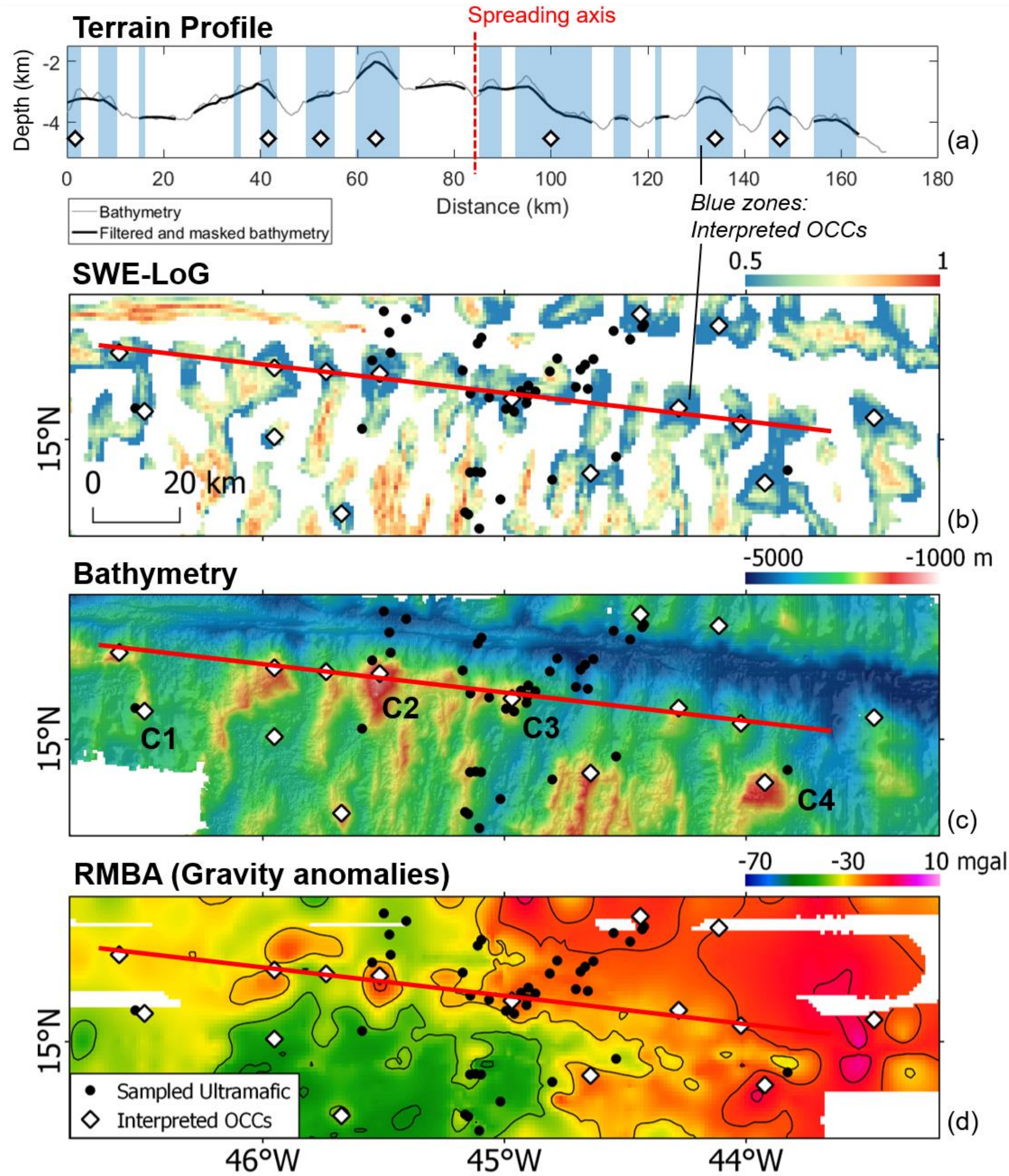

Figure 4 (a) Terrain profile of a cross-section at 15° N segment (bold red line on (b)). The LoG filter has smoothed terrain and masked-out bathymetric lows by eliminating concave upward areas. Interpreted OCCs and potential OCC zones from (b) are plotted as diamonds and 'blue zones' respectively. (b) SWE, masked with LoG filter. Interpreted OCCs are compared to both bathymetry (c), and Residual Mantle Bouguer Anomaly (RMBA) computed from gravity anomalies (d) (Smith et al., 2008). Indicated OCCs that match with the presence of ultramafics in its surrounding are marked as C1, C2, C3, and C4. Sampled ultramafic locations are taken from Fujiwara et al. (2003).

5 Conclusions

We have developed an automatic terrain classification algorithm based on the shape, directionality, and curvature of high-resolution bathymetry data termed as “Slope-Weighted Eccentricity” (SWE). The terrains are classified into three different types: (1) Detachment terrain, where the SWE 0-0.65; (2) Extended terrain, where the SWE is 0.65-0.9, and; (3) Magmatic terrain, where the SWE is > 0.9. Detachment terrain defined by this algorithm generally has high RMBA values, implying thinner crust, and high numbers of earthquakes at the specified segment. This type of terrain hosts features with the omnidirectional trend, such as OCCs and local basins, while the magmatic terrain hosts features with bidirectional trend, such as linear abyssal hills. Meanwhile, the extended terrain represents a buffer zone where both omnidirectional and bidirectional trends exist, showing the transition from detachment to magmatic spreading or *vice versa*. We suggest that this automated interpretation will aid efficient classification of oceanic crust terrains. It will serve as a significant first step to unravel the evolution of a slow-spreading ridge through time before a more thorough geophysical and geochemical analysis. Observing its consistency with RMBA values, computed from gravity anomalies, the method has the potential to be applied to gravity and magnetic or other gridded geophysical data. Assessing the algorithm for potential field data will allow wider application, such as identifying structures at ocean-continent transition zones where the oceanic crust features have been buried.

Acknowledgements

High resolution bathymetry and gravity data are available through Smith et al. (2008). Declustered seismicity data is available through Olive and Escartín (2016). The algorithm at 3.1 and 3.2 was developed using MATLAB. Gaussian and Laplacian filters were applied through GETgrid application developed by GETECH, plc. This work is published as part of a post-graduate research program at the University of Leeds, funded by the Indonesian Endowment Fund for Education (LPDP).

References

Blackman, D.K., Canales, J.P., Harding, A., 2009. Geophysical signatures of oceanic core complexes. Geophysical Journal International 178, 593-613.

Bonatti, E., 1996. Long-lived oceanic transform boundaries formed above mantle thermal minima. Geology 24, 803-806.

Buck, W.R., 1988. flexural rotation of normal faults. Tectonics 7, 959-973.

Buck, W.R., Lavier, L.L., Poliakov, A.N.B., 2005. Modes of faulting at mid-ocean ridges. Nature 434, 719-723.

Cann, J., Blackman, D., Smith, D., McAllister, E., Janssen, B., Mello, S., Avgerinos, E., Pascoe, A., Escartin, J.J.N., 1997. Corrugated slip surfaces formed at ridge–transform intersections on the Mid-Atlantic Ridge. 385, 329.

Cann, J.R., Smith, D.K., Escartin, J., Schouten, H., 2015. Tectonic evolution of 200 km of Mid-Atlantic Ridge over 10 million years: Interplay of volcanism and faulting. Geochemistry, Geophysics, Geosystems 16, 2303-2321.

Cannat, M., Bideau, D., Bougault, H., 1992. Serpentinized peridotites and gabbros in the Mid-Atlantic Ridge axial valley at 15°37′N and 16°52′N. Earth and Planetary Science Letters 109, 87-106.

Cannat, M., Lagabrielle, Y., Bougault, H., Casey, J., de Coutures, N., Dmitriev, L., Fouquet, Y., 1997. Ultramafic and gabbroic exposures at the Mid-Atlantic Ridge: geological mapping in the 15°N region. Tectonophysics 279, 193-213.

Dannowski, A., Grevemeyer, I., Ranero, C.R., Ceuleneer, G., Maia, M., Morgan, J.P., Gente, P., 2010. Seismic structure of an oceanic core complex at the Mid-Atlantic Ridge, 22°19′N. Journal of Geophysical Research: Solid Earth 115.

Escartín, J., Cannat, M., 1999. Ultramafic exposures and the gravity signature of the lithosphere near the Fifteen-Twenty Fracture Zone (Mid-Atlantic Ridge, 14°–16.5°N). Earth and Planetary Science Letters 171, 411-424.

Escartín, J., Hirth, G., Evans, B., 1997. Effects of serpentinization on the lithospheric strength and the style of normal faulting at slow-spreading ridges. Earth and Planetary Science Letters 151, 181-189.

Escartín, J., Hirth, G., Evans, B., 2001. Strength of slightly serpentinized peridotites: Implications for the tectonics of oceanic lithosphere. Geology 29, 1023-1026.

Escartín, J., Smith, D.K., Cannat, M., 2003. Parallel bands of seismicity at the Mid-Atlantic Ridge, 12–14°N. Geophysical Research Letters 30.

Fujiwara, T., Lin, J., Matsumoto, T., Kelemen, P.B., Tucholke, B.E., Casey, J.F., 2003. Crustal Evolution of the Mid-Atlantic Ridge near the Fifteen-Twenty Fracture Zone in the last 5 Ma. Geochemistry, Geophysics, Geosystems 4.

Huertas, A., Medioni, G., 1986. Detection of Intensity Changes with Subpixel Accuracy Using Laplacian-Gaussian Masks. IEEE Transactions on Pattern Analysis and Machine Intelligence PAMI-8, 651-664.

Lagabrielle, Y., Bideau, D., Cannat, M., Karson, J.A., MéVel, C., 1998. Ultramafic-Mafic Plutonic Rock Suites Exposed Along the Mid-Atlantic Ridge (10 N-30 N) Symmetrical-Asymmetrical Distribution and Implications for Seafloor Spreading Processes. GEOPHYSICAL MONOGRAPH-AMERICAN GEOPHYSICAL UNION 106, 153-176.

Lavier, L.L., Roger Buck, W., Poliakov, A.N.B., 1999. Self-consistent rolling-hinge model for the evolution of large-offset low-angle normal faults. Geology 27, 1127-1130.

MacLeod, C.J., Searle, R.C., Murton, B.J., Casey, J.F., Mallows, C., Unsworth, S.C., Achenbach, K.L., Harris, M., 2009. Life cycle of oceanic core complexes. Earth and Planetary Science Letters 287, 333-344.

MacLeod, C.J., Smith, D.K., Escartín, J., Banerji, D., Banks, G.J., Gleeson, M., Irving, D.H.B., Lilly, R.M., McCaig, A.M., Niu, Y., Allerton, S., 2002. Direct geological evidence for oceanic detachment faulting: The Mid-Atlantic Ridge, 15°45′N. Geology 30, 879-882.

Marr, D., Hildreth, E., 1980. Theory of edge detection. Proceedings of the Royal Society of London. Series B. Biological Sciences 207, 187-217.

McCaig, A.M., Harris, M., 2012. Hydrothermal circulation and the dike-gabbro transition in the detachment mode of slow seafloor spreading. Geology 40, 367-370.

Müller, R.D., Smith, W.H.F., 1993. Deformation of the oceanic crust between the North American and South American Plates. Journal of Geophysical Research: Solid Earth 98, 8275-8291.

Olive, J.-A., Escartín, J., 2016. Dependence of seismic coupling on normal fault style along the Northern Mid-Atlantic Ridge. Geochemistry, Geophysics, Geosystems 17, 4128-4152.

Reston, T.J., Ranero, C.R., 2011. The 3-D geometry of detachment faulting at mid-ocean ridges. Geochemistry, Geophysics, Geosystems 12.

Rona, P.A., Widenfalk, L., Boström, K., 1987. Serpentinized ultramafics and hydrothermal activity at the Mid-Atlantic Ridge crest near 15°N. Journal of Geophysical Research: Solid Earth 92, 1417-1427.

Schroeder, T., Cheadle, M.J., Dick, H.J.B., Faul, U., Casey, J.F., Kelemen, P.B., 2007. Nonvolcanic seafloor spreading and corner-flow rotation accommodated by extensional faulting at 15°N on the Mid-Atlantic Ridge: A structural synthesis of ODP Leg 209. Geochemistry, Geophysics, Geosystems 8.

Sinton, J.M., Detrick, R.S., 1992. Mid-ocean ridge magma chambers. Journal of Geophysical Research: Solid Earth 97, 197-216.

Smith, D.K., Cann, J.R., Escartín, J., 2006. Widespread active detachment faulting and core complex formation near 13° N on the Mid-Atlantic Ridge. Nature 442, 440-443.

Smith, D.K., Escartin, J., Cannat, M., Tolstoy, M., Fox, C.G., Bohnenstiehl, D.R., Bazin, S., 2003. Spatial and temporal distribution of seismicity along the northern Mid-Atlantic Ridge (15°–35°N). Journal of Geophysical Research: Solid Earth 108.

Smith, D.K., Escartín, J., Schouten, H., Cann, J.R., 2008. Fault rotation and core complex formation: Significant processes in seafloor formation at slow-spreading mid-ocean ridges (Mid-Atlantic Ridge, 13°–15°N). Geochemistry, Geophysics, Geosystems 9.

Smith, D.K., Tolstoy, M., Fox, C.G., Bohnenstiehl, D.R., Matsumoto, H., J. Fowler, M., 2002. Hydroacoustic monitoring of seismicity at the slow-spreading Mid-Atlantic Ridge. Geophysical Research Letters 29, 13-11-13-14.

Tucholke, B.E., Behn, M.D., Buck, W.R., Lin, J., 2008. Role of melt supply in oceanic detachment faulting and formation of megamullions. Geology 36, 455-458.

Watson, G.S., 1965. Equatorial Distributions on a Sphere. Biometrika 52, 193-201.

Woodcock, N.H., 1977. Specification of fabric shapes using an eigenvalue method. GSA Bulletin 88, 1231-1236.